Title

Fluid migration in low-permeability faults driven by decoupling of fault slip and opening

Journal
Nature Geoscience, 15(9)

ISSN
1752-0894

Authors
Cappa, Frédéric
Guglielmi, Yves
Nussbaum, Christophe
et al.

Publication Date
2022-09-01

DOI
10.1038/s41561-022-00993-4

Decoupling between slip and opening drives high-pressure fluid migration in shale faults

Frédéric Cappa[1,2,*], Yves Guglielmi[3], Christophe Nussbaum[4], Louis De Barros[1], and Jens Birkholzer[3]

[1] Université Côte d'Azur, CNRS, Observatoire de la Côte d'Azur, IRD, Géoazur, Sophia Antipolis, France
[2] Institut Universitaire de France, Paris, France
[3] Energy Geosciences Division, Lawrence Berkeley National Laboratory, Berkeley, California, USA
[4] Federal Office of Topography, Swisstopo, St-Ursanne, Switzerland

*e-mail to: frederic.cappa@univ-cotedazur.fr

High-fluid pressures can penetrate faults and diffuse through channels while activating slip. Here, we use observations from a cross-borehole fluid injection experiment in a low permeability shale-bearing fault to show that the fault slips and opens prior to fluid pressure build-up. Reproducing the data with numerical models, we find that the fluid migrates in the fault only after the fault fails and primarily slips beyond the pressurized area. This is creating potential hydraulic pathways that are then widely opened by a large effective normal stress decrease that overtakes the shear-induced dilation. These results provide new *in situ* constraints on mixed rupture processes which drive the fluid migration in low permeability faults.

Fluids can reactivate tectonic faults and have the potential to cause earthquakes, as observed in both natural seismic swarms[1,2] and energy production activities[3,4]. Increase in fluid pressure can also trigger aseismic slip on faults[5,6]. At the same time, hydraulic fault properties are an important factor as the evolution of permeability and porosity is coupled with slip, and a consequence of this interaction is the variation of fluid pressure[7,8].

Recent works have shown that even low permeability faults can serve as a conduit for transmission and increase of fluid pressure because the fault permeability can transiently increase during slip[9,10]. However, in the absence of *in situ* continuous measurements of fluid pressure and deformation in faults, important questions remain, such as how fluid pressure migrates along faults, and how the fault responds.

Here, using an *in situ* cross-borehole experiment with controlled fluid injection into a low permeability shale fault zone ($k_0 \sim 10^{-17}$ m^2,[11]), we directly measured the evolution of fluid pressure and fault displacements (Fig. 1) at two vertical boreholes, spaced about 3 m horizontally. This meter-scale experiment was developed at a depth of 340 m in the Mont Terri Underground Research Laboratory, Switzerland[12] (Supplementary Fig. S1). Reproducing the observations with hydromechanical models, we track the fluid migration in association with fault deformation. Results give insights into how the decoupling between slip and opening, as well as the shear stress perturbation occurring outside the pressurized zone, control the fluid migration over the fault.

Controlled-injection fault activation

The experiment was conducted in a 1.5–3 m thick seismically-inactive thrust fault zone with a mean orientation of N°045 in dip direction, a dip of 45°, and a slip offset of a few meters[11] (Fig. 1a, and Supplementary Figs. S1 and S2). During the experiment, pressurized water was injected for 645 s with step-increasing rates into a 2.4-m-long packer-isolated borehole interval spanning the main slip plane of the fault zone. The fluid pressure, the fault-normal (opening) and the fault-parallel (slip) displacements were recorded at both the injection and monitoring points with a specially designed borehole (SIMFIP) probe[13] (see Methods) (Fig. 1a and Supplementary Fig. S2), while the flowrate was only monitored at the injection point. The experiment was conducted in a pressure-controlled mode to maintain a quasi-constant pressure value during each step. Thus, the injection flowrate corresponds to the rate of fluid flow into the fault required to achieve and maintain the target pressure. Prior to the experiment, the state of stress was estimated at σ_1 = 6-to-7 MPa (subvertical), σ_2 = 4-to-5 MPa and σ_3 = 0.6-to-2.9 MPa (subhorizontal), using a combination of geological data, borehole hydromechanical measurements, and modeling[14-16]. The initial fluid pressure in the packed-off interval before injection was measured at 0.5 MPa. The temperature is constant (15.6°C) in the boreholes during the experiment.

At the injection point, the fluid pressure was increased step-by-step from the initial value of 0.5 MPa to a maximum value of 5.4 MPa (Fig. 1b). This maximum value represents an extreme fluid pressurization relative to the local stress conditions. As the pressure increased in the injection borehole, no change was detected until a complex evolution of fault deformation and fluid pressure response started at the injection point and then at the monitoring point (Figs. 1b and 1c), about 555 s into the experiment. The fault is reactivated, implying a sudden enhancement of the fault's permeability and fluid flow. No seismic event was observed, the fault displacements thus appear aseismic. We examine here in detail the temporal sequence of processes at the two measuring points (Supplementary Fig. S3). At the injection, first, the fault slip initiates at 555 s, followed by rapid fault opening at 568 s, and flowrate increase (0 to 33.8 l/min) at 572 s (Fig. 1d). Then, the fluid pressure decreases from the peak to a steady-state value of 4.2 MPa. Fault slip accelerates with fluid flow, and then decelerates when flowrate and pressure become constant and fault opening stabilizes. The slip increased to about 18.7 μm, and the opening up to 19.7 μm. A secondary phase of fault closing followed by opening is observed from 628 to 632 s. At the monitoring point, first, the fault slip initiates at 574 s after the beginning of injection, followed by fault opening at 587 s (Fig. 1e). No fluid pressure change was detected until 31 μm of fault slip, 5 μm of fault opening, about 597 s into the experiment. Thus, at the monitoring point, the fluid pressure starts to increase 23 s after the fault starts to slip. The fluid pressure reaches a maximum value of 4.17 MPa at 623 s. The fluid pressurization occurs at a rate of 0.16 MPa/s. This phase of pressurization is associated with fault closing (10.7 μm from 597 to 618 s) and slip at a slower rate toward the peak value (58.5 μm at 622 s). After the peak of pressurization at the monitoring point, the fluid pressure slightly decreases and stabilizes at a value of 3.85 MPa. This phase is associated with a fault opening of 24 μm from 618 to 645 s. Meanwhile, there is a decrease of fault slip of 20 μm, from 58.5 μm at 622 s to 38.5 μm at 645 s.

From the evolution of flowrate, fluid pressure and slip between the two measuring points, we estimate a pressure migration speed at 0.174 m/s, and a rupture propagation at a speed of 0.228 m/s. These observations demonstrate that the fault initially failed in shear with slip preceding the fluid migration, which is slower (~24%) than the rupture velocity. Then, a large fault opening, that is poorly coupled to slip, occurred and resulted in sufficient permeability enhancement ($\Delta k \sim 2.78 \times 10^5$ m^2 from its initial pre-slip value of $\sim 10^{-17}$ m^2) over a large enough patch of the fault to generate connectivity between the two boreholes. The increase in fluid pressure came after this sequence of fault slip and opening.

Coupled modeling of fault deformation and fluid flow

To investigate the process responsible for the dynamic evolution of the hydraulic connection between the two boreholes and the sudden increase in fluid pressure measured at the monitoring point, we developed a three-dimensional hydromechanical model of this *in situ* experiment (see Methods). The model simulates the fluid flow, slip and opening along a planar fault with a dip of 45° in an elastic and impervious medium (Fig. 1a). The initial hydromechanical properties, measured in the laboratory and *in situ*[15,17], are uniform over the fault (Supplementary Table S1). Before injection, the *in situ* stresses and fluid pressure are initialized over the fault. We used the gradual step-by-step pressurization measured at injection as loading path (Fig. 1b). During injection, fluid pressure (p) and effective normal stress (σ_n-p) evolve over the fault, and modify the fault strength $\tau = c + \mu \cdot (\sigma_n - p)$. Once a fault rupture initiates, the friction coefficient (μ) is governed by a linear slip-weakening law[18], while the fault cohesion (c) instantaneously falls to zero (see Methods). Fluid flow is governed by the modified cubic law[19], with effective stress- and shear dilation-induced permeability change on the fault (see Methods). We compare three permeability evolution (Fig. 2a), including (1) a model with constant permeability, (2) a model with a variable permeability activated from the start of injection, and (3) a model with a variable permeability activated only in the ruptured part of the fault (see more details in the Methods section).

The measured fluid pressure evolution is reproduced by the numerical solution when the fault first fails and slips while activating permeability change (Figs. 2a and 2b), whereas models with a constant or variable permeability from the start of injection do not capture the data. The injection of fluid increases the pressure, which weakens the fault and initiates failure. Once the fault fails and starts slipping, the fluid enters the ruptured parts and induces a decrease of effective normal stress, causing an intense fault opening and slip acceleration, consistently with field data (Fig. 2b). The model fits well the last phases of rapid increase of fluid pressure and stabilization at a maximum value (~4 MPa). Model results (Fig. 3, and Supplementary Fig. S4) also show that the fluid pressure front follows the migration of peak shear stress where rupture occurs. Shear stress increases within a highly localized zone at the rim of the region of fluid pressurization. In this high stressed zone, the stored energy is released when the shear stress exceeds strength and the fault fails, resulting in slip propagation and creation of hydraulic pathways. The shear stress perturbation arising from fault slip develops beyond the pressure front (Fig. 3a), and gradually drops from the peak to background value (Figs. 3b-f). At the end of injection, the fault area where the stress perturbation occurs is about 6 times the size of the pressurized area (Fig. 3f). This result is consistent with previous modeling studies, suggesting that increased shear stress and friction weakening drive slip beyond the pressure front[20,21] (Supplementary Figs. S5 and S6). By varying the model parameters (Supplementary Fig. S7), we also show that the initiation time of fluid pressurization at the monitoring point is strongly influenced by the amount of frictional weakening (Supplementary Fig. S7B). To match the fluid pressure observed at the monitoring point, the fault weakens significantly with frictional strength drop of 83.3 %.

Comparison of the data with the model solutions shows that the data fit is good for the fluid pressure, except the displacements (Figs. 2a and 2b). Although modelled displacements capture the main features of the observed signals, some differences in shape and amplitude arise because of simplified model assumptions used to represent the natural fault zone such as a single planar fault geometry and uniform hydromechanical parameters, and because we did not account for the off-fault deformation on surrounding fractures. In addition, the exact process responsible for the observed rapid changes in acceleration or deceleration of fault displacements remains elusive. They could reflect interactions between the fault weakening induced by fluid pressurization, frictional stability of shales at low effective stress, and variable material properties[22,23]. The time lag observed between the change in fluid pressure and fault opening is reproduced slightly differently by the model that does not consider the storage effect associated with the monitoring interval. Indeed, in the field, the pressure front propagating along the fault enters the larger monitoring interval of the borehole, which induces a delayed pressurization at the pressure sensor. Despite the model simplifications, our numerical results show two phenomena that can be compared to observations: (1) a decoupling between fault slip and opening, and (2) a rapid fluid pressurization rate initiating at failure. Importantly, shear stress increase at the rupture front and frictional weakening with increasing slip offer an efficient mechanism for rupture propagation, permeability enhancement and the rapid transmission of high-fluid pressures within low permeability faults.

Implications for fluid pressure migration along faults

This study demonstrates that fluid pressure migration along low permeability faults is driven by rupture growth through stress perturbation ahead of the pressurized zone. This behavior is different from the fluid diffusion in permeable and porous media[24]. The most pronounced change in behavior occurs when the fault rupture increases permeability and fluid flows in the preferential direction of fault slip. Our results are consistent with previous laboratory-sized experiments on sawcut rock surfaces, which showed that rupture is a necessary condition to allow fluid flow in low permeability faults[25].

Our observations also provide clear *in situ* constraints on the physics underlying fault permeability enhancement in shales. Once failure occurs, a large increase in permeability and significant fluid migration can occur in the fault, now mainly driven by fault opening as a result of a strong decrease in effective normal stress. At this point, the fault is at rupture but the contribution of dilation induced by slip to permeability enhancement is minor. This fault response demonstrates that a mixed-mode rupture mechanism favored by a combination of slip propagation and opening explains such rapid fluid migration at high pressure and the apparent decoupling between fault slip and opening in low permeability shale formations[9].

Beyond improving our fundamental knowledge about the relationship between fault slip, opening and fluid migration in a shale fault, the mechanisms observed in this experiment could also be beneficial to understand how induced seismicity, and in a broader context, natural earthquakes are triggered by fluid perturbations operating in the Earth's crust, since there appears to be a clear link between permeability increase from slip and reduction in effective normal stress. This process is efficient for the transmission of high-fluid pressures at fast rates over sufficiently large sections of a fault that can potentially transition from aseismic creep to seismic slip. Fluid pressurization in low permeable faults can also increase shear stress at the periphery of the dilatant slip zone and promotes earthquake nucleation in the neighboring asperities or segments.

Methods

Methods and any associated references are available in the online version of the paper.

References

1. Shelly, D.R. et al. Fluid-faulting evolution in high definition: Connecting fault structure and frequency-magnitude variations during the 2014 Long Valley Caldera, California, earthquake swarm. *J. Geophys. Res.,* **121**, 1776–1795, 10.1002/2015JB012719 (2016).
2. Ross, Z.E. et al. 3D fault architecture controls the dynamism of earthquake swarms. *Science*, **368**(6497), 1357-1361, doi:10.1126/science.abb0779 (2020).
3. Ellsworth, W.L. Injection-induced earthquakes. *Science,* **341**, 6142, 10.1126/science.1225942 (2013).
4. Keranen, K.M. & Weingarten, M. Induced seismicity. *Annu. Rev. Earth Planet. Sci.*, **46**, 149-174, 10.1146/annurev-earth-082517-010054 (2018).
5. Guglielmi, Y. et al. Seismicity triggered by fluid injection-induced aseismic slip. *Science*, **348**, 1224, 10.1126/science.aab0476 (2015).
6. Wei, S. et al. The 2012 Brawley swarm triggered by injection-induced aseismic slip. Earth Planet. Sci. Lett., **422**, 115-125, 10.1016/j.epsl.2015.03.054 (2015).
7. Sibson, R.H. Conditions for fault-valve behaviour. *Geol. Soc. Lond. Spl. Publ.,* **54**, 15–28 (1990).
8. Zhu, W. et al. Fault valving and pore pressure evolution in simulations of earthquake sequences and aseismic slip. *Nature Communications*, **11**:4833, 10.1038/s41467-020-18598-z (2020).
9. Guglielmi, Y. et al. In situ observations on the coupling between hydraulic diffusivity and displacements during fault reactivation in shales. *J. Geophys. Res.*, **120**, 10.1002/2015JB012158 (2015).
10. Wu, W. et al. Permeability evolution of slowly slipping faults in shale reservoirs. *Geophys. Res. Lett.*, **44**, 11,368-11,375, 10.1002/2017GL075506 (2017).
11. Wenning, Q.C. et al. Shale fault zone structure and stress dependent anisotropic permeability and seismic velocity properties (Opalinus Clay, Switzerland). *J. Struct. Geol.*, **144**, 104273, 10.1026/j/jsg.2020.104273 (2020).
12. Thury, M. & Bossart, P. The Mont Terri rock laboratory, a new international research project in a Mesozoic shale formation, in Switzerland. *Engineering Geology*, **52**(3–4), 347-359 (1999).
13. Guglielmi, Y. et al. ISRM Suggested Method for Step-Rate Injection Method for Fracture In Situ Properties (SIMFIP): Using a 3-components borehole deformation sensor. *Rock Mech. Rock Eng.*, **47**, 10.1007/s00603-013-0517-1 (2014).
14. Martin, C.D. & Lanyon, G.W. Measurement of in situ stress in weak rocks at Mont Terri Rock Laboratory, Switzerland. *Int. J. Rock Mech. Min. Sci.*, **40**(7–8), 1077–1088 (2003).
15. Guglielmi, Y. et al. Complexity of fault rupture and fluid leakage in shale: insights from a controlled fault activation experiment. *J. Geophys. Res.*, **125**, 10.1029/2019JB017781 (2020).
16. Guglielmi, Y. et al. Estimating perturbed stress from 3D borehole displacements induced by fluid injection in fractured or faulted shales. *Geophys. J. Int.*, **221**, 10.1093/gji/ggaa103 (2020).
17. Orellana, L.F. et al. Contrasting mechanical and hydraulic properties of wet and dry fault zones in a proposed shale-hosted nuclear waste repository. *Geophys. Res. Lett.*, **46**, 10.1029/2018GL080384 (2019).
18. Ida, Y. Cohesive force across the tip of a longitudinal-shear crack and Griffith's specific surface energy *J. Geophys. Res.*, **77**(20), 3796-3805 (1972).
19. Witherspoon, P.A. et al. Validity of cubic law for fluid flow in a deformable rock fracture. *Water Resour. Res.*, **16**, 1016-1024 (1980).
20. Cappa, F. et al. On the relationship between fault permeability increases, induced stress perturbation, and the growth of aseismic slip during fluid injection. *Geophys. Res. Lett.*, **45**, 10.1029/2018GL080233 (2018).

21. Bhattacharya, P. & Viesca, R.C. Fluid-induced aseismic fault slip outpaces pore-fluid migration. *Science*, **364**, 10.1126/science.aaw7354 (2019).
22. Scuderi, M.M. et al. Frictional stability and earthquake triggering during fluid pressure stimulation of an experimental fault. *Earth Planet. Sci. Lett.* **477**, 10.1016/j.epsl.2017.08.009 (2017).
23. Scuderi, M.M. & Collettini, C. Fluid injection and the mechanics of frictional stability of shale-bearing faults. *J. Geophys. Res.* **123**, 10.1029/2018JB016084 (2018).
24. Wang, H.F. Theory of Linear Poroelasticity, 287 pp., Princeton Univ. Press. (2000).
25. Rutter, E.H. & Hackston, A. On the effective stress law for rock-on-rock frictional sliding, and fault slip triggered by means of fluid injection. *Philosophical Transactions of the Royal Society of London*, **375**, 10.1098/rsta.2016.0001 (2017).

Acknowledgments

This work has been supported by the Federal Office of Topography, Swisstopo, and by the U.S. Department of Energy (Spent Fuel and Waste Science and Technology Research Group). F. Cappa acknowledges support from the Institut Universitaire de France. We thank E. Dunham, R.M. Pollyea and one anonymous reviewer for constructive comments.

Authors contributions

F.C. and Y.G. designed the study. Y.G. and C.N. performed the experiment. F.C. performed the numerical simulations. All authors contributed to the analysis of the data and simulations, and preparation of the manuscript.

Competing interests

The authors declare no competing interests.

Additional information

Supplementary information is available in the online version of this paper. All experimental data used in producing the figures 1b and 1c of this manuscript are available in the supplementary information.

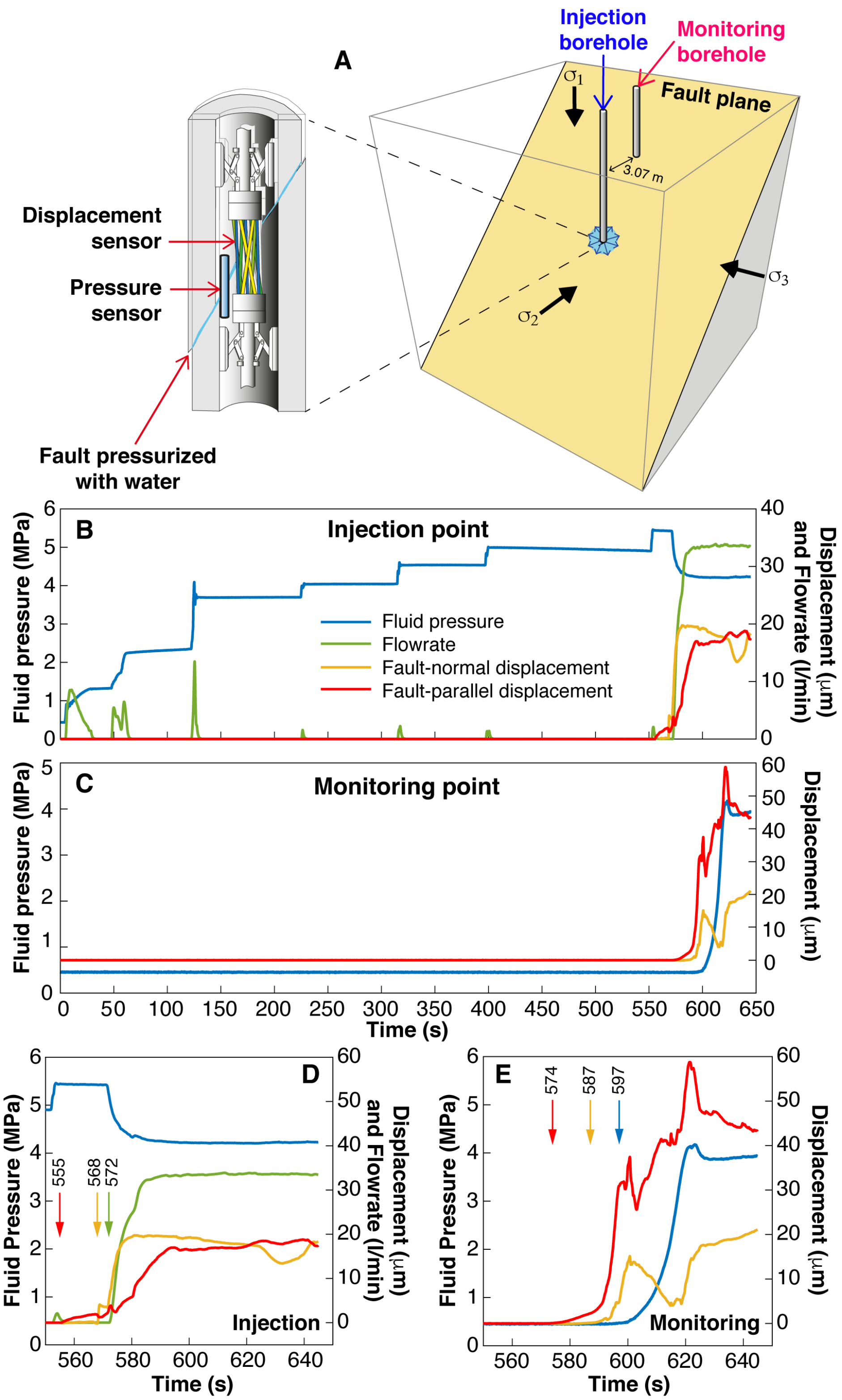

Figure 1. Experiment setting and in situ data. a, Geometry of the experimental zone at a depth of 340 m below the Earth's surface in the Mont Terri Underground Research Laboratory in Switzerland, and numerical model schematic. Fluid is injected through the open section of the injection borehole into the fault. A borehole probe (SIMFIP) was used to simultaneously measure the fault displacement (fault-parallel ("slip") in red, and fault-normal ("opening") in gold) and fluid pressure (blue) at the **b**, injection and **c**, monitoring points. Flowrate (green) is measured at injection. **d** and **e**, Close-up view of the time window 550 to 645 s.

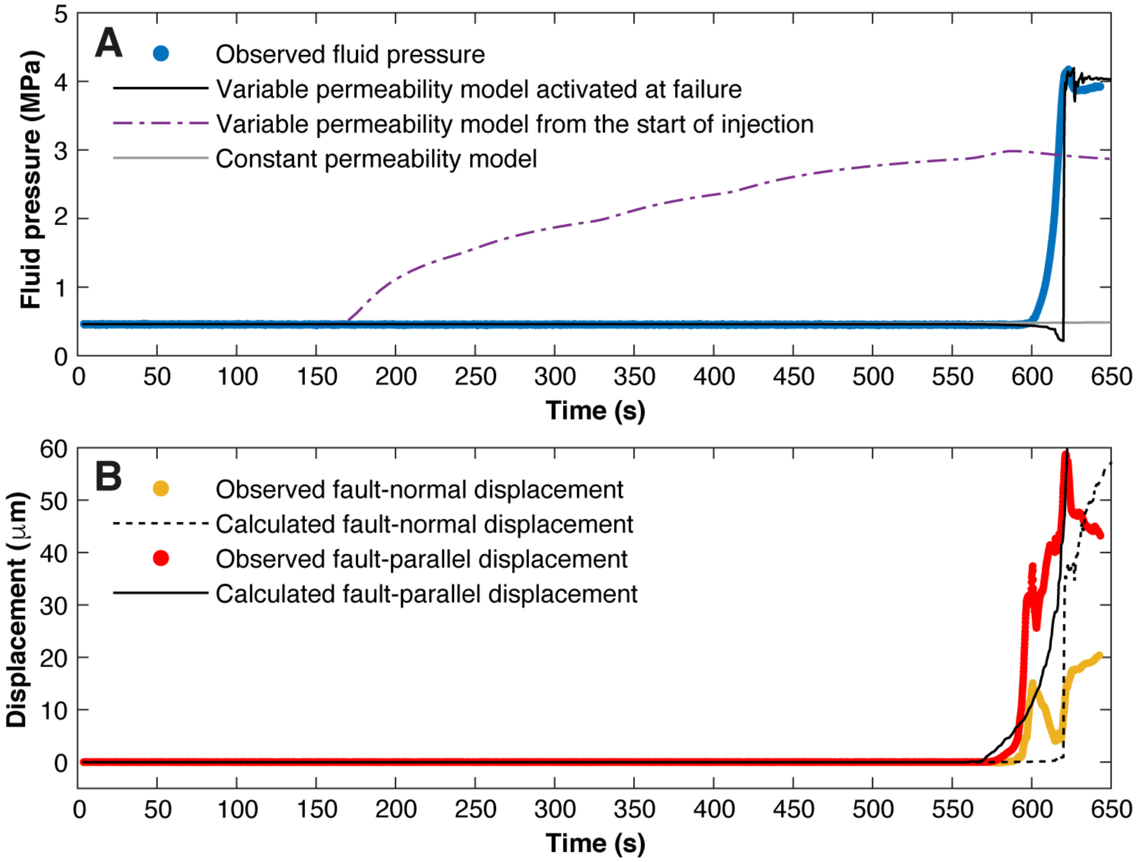

Figure 2. Comparison of observed and modeled fluid pressure and fault displacements at the monitoring point in response to fluid injection. **a**, Best-fit numerical solution for fluid pressure calculated with a variable permeability model activated at failure (black). For comparison, the fluid pressure calculated with a variable permeability model from the start of injection (purple) and a constant permeability (grey) is presented. **b**, Model-predicted fault displacements for the variable permeability model activated at failure.

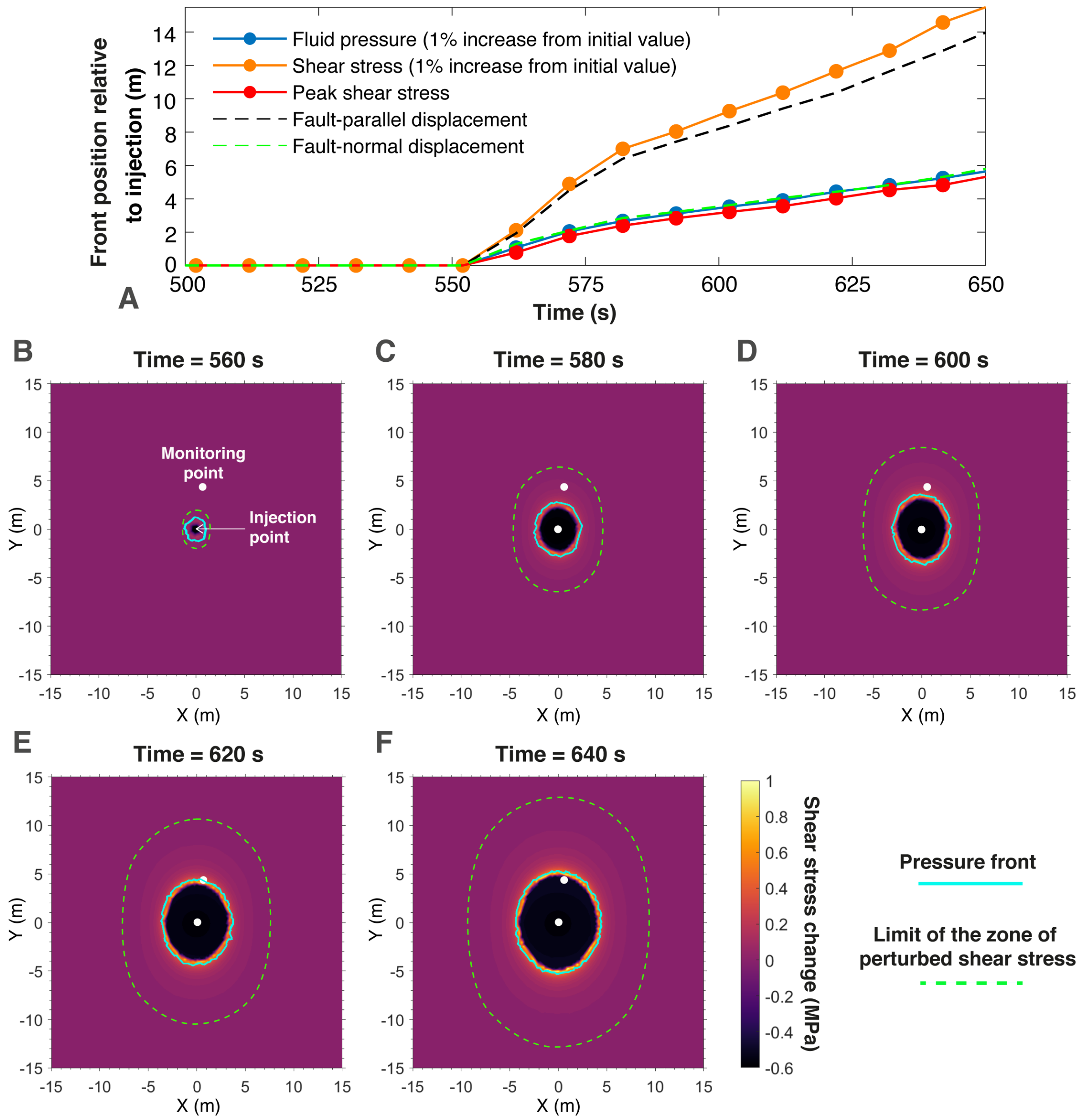

Figure 3. Spatio-temporal evolution of fault behavior. a, Time evolution of the fronts of fluid pressure, fault displacements, and shear stress. **b-f**, Spatial distributions of the change in shear stress relative to the initial value at the indicated times (560, 580, 600, 620 and 640 s) for the best-fit numerical solution. On each snapshot, the cyan contour represents the locations of the fluid pressure front (1% increase from initial value) and the dashed green contour marks the limit of the zone of perturbed shear stress.

Methods

Monitoring fault movements with a SIMFIP borehole probe during the fluid injection field experiment

In the Mont Terri experiment (Supplementary Fig. S1), two SIMFIP borehole probes allow the simultaneous monitoring of fluid pressure in the fault and three-dimensional displacements of the fault[13]. A 2.4 m-long sealed interval is isolated in an open hole using two inflatable rubber packers (Supplementary Figs. S2a and S2b). A 0.49 m long and 0.1 m diameter pre-calibrated aluminum cage located between the two packers is clamped on the borehole wall on both sides of the existing fault plane. When clamped, the cage is disconnected from the straddle packer system. When the fault is moving as a result of the fluid injection into the interval, the cage monitors the three-dimensional displacement tensor and the three rotations of the upper anchor of the cage relatively to the lower anchor. The maximum displacement range of the deformation cage is 0.7 and 3.5 mm in the axial and radial directions of the borehole, respectively, and the accuracy is $\pm 5 \times 10^{-6}$ m. A compass set on the probe provides the orientation of measurements with 0.1° accuracy. In this paper, the displacements are rotated into tangential (i.e., parallel) and normal (i.e., perpendicular) displacements of the fault. The displacement data are continuously logged together with pump parameters (pressure and flowrate), as well as temperature and pressure in the borehole above, between and below the packers. The pressure sensors allow for measurements over a pressure range from 0 to 10 MPa, with a 0.001 MPa accuracy. The accuracy of the temperature sensors is 0.1°C.

During the hydraulic injection test, the injection pressure is controlled by an engine pump while flowrate, pressure, temperature and displacement variations from the two SIMFIP probes, respectively installed in the injection borehole and in the monitoring borehole, are monitored with the same acquisition station. The sampling frequency is 500 Hz.

Numerical modelling: assumptions and parameters

To investigate the origin of the rapid increase in fluid pressure measured at the monitoring point and the hydraulic connection between the two boreholes, we have used a three-dimensional distinct element code[26]. This numerical code was successfully used to model fluid injections in faults and fractured rocks[9,20,27]. The model simulates the fluid flow and the evolution of the mechanical displacements along a single fault plane to the step-by-step pressurization boundary condition imposed at the injection point (Fig. 1b and Supplementary Fig. S4a). A sensitivity analysis was also conducted to address the influence of the faults' hydromechanical properties (mainly frictional and hydraulic parameters; Supplementary Fig. S7) on its rupture and hydraulic behavior. In this modeling, we focus on reproducing the hydromechanical response of the fault at the monitoring point.

Details about the numerical code are provided in Cappa et al. (2018)[20] and Wynants-Morel et al. (2020)[27]. The model employs the modified cubic law[19] (eq. 1) for fluid flow along a smooth deformable fault (i.e., no roughness), and fault slip is initiated based on the Mohr-Coulomb failure criterion ($\tau = c + \mu \cdot \sigma_n'$, where τ is the shear stress at which slip initiates; c is the cohesion, σ_n' is the effective normal stress, i.e., total normal stress, σ_n, minus fluid pressure, p; and μ is the friction coefficient)[28]. When the fault slips, a linear slip-weakening friction law (eq. 5) is used[18]. A frictional stress-dependent permeability is applied to calculate the fluid pressure diffusion in the slipping patches of the fault. In this model, fluid flow is thus activated at failure and occurs only in the ruptured part of the fault (i.e., no fluid flow in the unruptured parts).

The fluid flow over the fault is computed as follows:

$$q = -\frac{{b_h}^3 \cdot w}{12\mu_f}\nabla p \qquad (1)$$

where q is the volumetric flow rate (m^3/s), w denotes the fault width (m), μ_f is the fluid dynamic viscosity (Pa.s), ∇p is the fluid pressure gradient (Pa/m). The fault hydraulic aperture (b_h in m) varies with the effective normal stress and shear-induced dilation:

$$b_h = b_{ho} - \frac{\Delta\sigma'_n}{k_n} + \Delta u_s \cdot \tan\psi \qquad (2)$$

where b_{ho} (m) is the initial hydraulic aperture at failure initiation, $\Delta\sigma_n'$ is the increment in effective normal stress (σ_n - p) (Pa), k_n is the fault normal stiffness (Pa/m), Δu_s (m) is the slip increment, and ψ is the dilation angle (°). Dilation occurs only as the fault slips. Assuming smooth fault surfaces, the hydraulic aperture is linked to the permeability, k, (m^2) as follows[19]:

$$k = \frac{b_h^2}{12} \qquad (3)$$

The fluid pressure in the deformable fault follows a diffusion equation:

$$\frac{\delta p}{\delta t} = \frac{{b_h}^2 K_f}{12\mu_f}\nabla^2 p - \frac{K_f}{b_h}\frac{\delta b_h}{\delta t} \qquad (4)$$

where K_f is the fluid bulk modulus (Pa) and t is the time. Thus, the change in pressure is a result of fluid flow (the first term in equation 4) and mechanical deformation (the second term in equation 4).

The distinct element method[29,30] is used to calculate displacements along the fault and rotations of rock blocks that surrounds it. On the fault, linear stress-displacement relations govern the elastic motions, in both the parallel and perpendicular directions.

The model is discretized with tetrahedral zones. The finite volume method is used to calculate stresses and strains in the rock blocks. The code uses an explicit time-marching procedure[26]. Within each time step, the two-way coupling calculation is sequentially iterative, and proceeds by performing a fluid calculation step and then some mechanical calculation steps to achieve a hydromechanical equilibrium. Thus, the permeability of the fault is affected by the mechanical deformation, and the fluid pressure affects the mechanical computation at each time step.

We built a model (60 m × 60 m × 60 m) which considers fluid injection into a single fault plane with a dip angle of 45° in a homogeneous elastic and impervious medium (Fig. 1a). The fault zone geometry is inferred from previous geological studies[31]. To calibrate the model, we used the injection pressure measured from the experiment as the input data (Fig. 1b), and compared the monitoring pressure obtained from the numerical solution and experimental data (Figs. 1c, 2a, and Supplementary Figs. S4 and S5).

The fault hydromechanical properties and the rock elastic properties were taken from previous studies[16] (Supplementary Table S1). Before injection, the initial properties are uniform over the fault. For the slip-weakening friction law[18], we use the following frictional parameters, μ_s = 0.6, μ_d = 0.1, and d_c = 150 microns to model the evolution of the friction coefficient (μ) as a function of the amount of slip (D):

$$\mu = \begin{cases} \mu_s - (\mu_s - \mu_d)\frac{D}{\delta_c} & D < \delta_c \\ \mu_d & D > \delta_c \end{cases} \quad (5)$$

These values fall within the range of frictional parameters measured in laboratory tests at low stress conditions and slow slip rates on the fault samples collected in deep boreholes used for the present injection experiment[17]. It is important to note that a very low dynamic friction coefficient (μ_d) is required in the model to reproduce the rapid pressure build-up and the mixed-mode deformation mechanism with fault slip and opening observed at the monitoring point

The first modelling stage consists of a comparison of different fluid flow modes to evaluate capabilities of each mode to reproduce the fluid pressure evolution observed at the monitoring point (Fig. 2a, and Supplementary Fig. S4). In this application, we tested three models:

(1) A constant permeability model (i.e., constant hydraulic aperture, $b_h = b_{ho}$);

(2) A variable permeability model (i.e., hydraulic aperture changes according to Equation 1) activated from the start of injection;

(3) A variable permeability model activated at failure (i.e., Equation 1 and frictional stress-dependent permeability model activated at failure as described above, when Δu_s >0).

References

26. Itasca Consulting Group, Inc. 3DEC 3-dimensional distinct element code. Minneapolis: ICG (2016).
27. N. Wynants-Morel, F. Cappa, L. De Barros, J.P. Ampuero, Stress Perturbation From Aseismic Slip Drives The Seismic Front During Fluid Injection In A Permeable Fault, *J. Geophys. Res.*, **125**, e2019JB019179, doi:10.1029/2019JB019179 (2020).
28. J.C. Jaeger, N.G.W. Cook, Fundamentals of Rock Mechanics, *Chapman and Hall*, London, U.K. (1979).
29. Cundall PA, Strack ODL, A discrete numerical model for granular assemblies, *Geotechnique*, **29**(1):47-65. doi: 10.1680/geot.1979.29.1.47 (1979)
30. Cundall, P. A. Formulation of a three-dimensional distinct element model—Part I. A scheme to detect and represent contacts in a system composed of many polyhedral blocks. *Int. J. Rock Mech. Min. Sci. Geomech. Abs.*, **25**(3), 107–116. https://doi.org/10.1016/0148-9062(88)92293-0 (1988)
31. C. Nussbaum, P. Bossart, F. Amann, C. Aubourg. Analysis of tectonic structures and excavation induced fractures in the Opalinus Clay, Mont Terri underground rock laboratory (Switzerland). *Swiss J. Geosci.*, **104**, 187-210 (2011).